Tectonophysics xxx (2011) xxx–xxx

Contents lists available at SciVerse ScienceDirect

Tectonophysics

journal homepage: www.elsevier.com/locate/tecto

The 2008 Yutian normal faulting earthquake (Mw 7.1), NW Tibet: Non-planar fault modeling and implications for the Karakax Fault

Masato Furuya *, Takatoshi Yasuda

Department of Natural History Sciences, Graduate School of Science, Hokkaido University, N10W8, Kita-ku, Sapporo 060-0810, Japan

ARTICLE INFO

Article history:
Received 28 April 2011
Received in revised form 6 September 2011
Accepted 8 September 2011
Available online xxxx

Keywords:
Karakax Fault
Normal faulting earthquake
Synthetic aperture radar
Northwest Tibet
Triangular dislocation element
Non-planar fault

ABSTRACT

The ENE striking Altyn-Tagh Fault and the WNW striking Karakax Fault are two major strike–slip fault systems in northern Tibet, and form a prominent ~2000 km long fault system. The 2008 Yutian normal faulting earthquake (Mw 7.1) struck near the southern edge of the Tarim Basin, where the two fault systems converge. While there are numerous NS-trending normal faults particularly in southern Tibet, their tectonic origins have remained contentious. Based on crustal deformation data sets obtained from synthetic aperture radar (SAR) as well as aftershock distribution, we developed a non-planar fault source model for the 2008 Yutian earthquake that exhibits a large normal-fault slip on a west-dipping surface with a nearly NS strike, thus suggesting a localized EW trending extensional stress field. The extensional stress was presumably generated at a step-over region of two NE-trending left-lateral strike–slip faults, which would probably belong to the Altyn-Tagh and Longmu–Gozha Co Fault Systems. In the epicentral area, there exists a fault scarp that coincides with the top edge of our fault model, and thus similar earthquakes must have occurred over geological time. Such normal faulting earthquakes must have been repeatedly suppressed the left-lateral slip behavior of the Karakax Fault. In addition, if the slip along the Altyn-Tagh Fault is transferred to the Longmu–Gozha Co Fault, which is SE across the normal fault system, the slip rate of the Karakax Fault would be less than that of the adjoining Altyn-Tagh Fault.

1. Introduction

While a variety of observations have shown that north–south (NS) striking normal faults are broadly distributed in Tibet (e.g., Armijo et al., 1986; Avouac and Peltzer, 1993; Elliot et al., 2010; Molnar and Lyon-Caen, 1989; Molnar and Tapponnier, 1978; Sun et al., 2008; Tapponnier and Molnar, 1977), it remains unclear why east–west (EW) extensions are generated over a wide area in Tibet. Molnar and Tapponnier (1978) proposed a gravitational spreading model, which considers that the thick crust cannot be supported by its mechanical strength and will tend to collapse. To account for the extensional stress as well as the compressional stress associated with the convergence between India and Asia, England and Houseman (1989) considered the thermal evolution of the thickened lithosphere and suggested a convective instability of the lower lithosphere and its subsequent replacement by the hot and light asthenosphere. In addition, noting the systematic changes in rift spacing from north to south, the overall similarities in the age of rift initiation, and the systematic NS trends in rift orientation, Yin et al. (1999) and Yin (2000) pointed out the importance of a regional boundary condition at a scale of thousands of kilometers. Recently, Copley et al. (2011) pointed out a clear contrast in the tectonic regime between northern and southern Tibet, considering the normal faulting in northern Tibet as minor, and indicated that a strong mechanical coupling of Indian lower crust in southern Tibet could explain the EW-extension in southern Tibet. The focus of this paper is not in the numerous normal faults in southern Tibet but in the rather localized normal faults in the northwestern Tibet.

On March 20, 2008 at 22:33 UTC, an earthquake (M7.2/USGS) struck the Yutian county, Xinjiang, China. The event was the largest normal faulting earthquake ever instrumentally recorded in northern Tibet (Fig. 1; Ekström et al., 2005; Elliot et al., 2010; Global Centroid Moment Tensor project, 2008). Hence, the 2008 Yutian earthquake provides us with an opportunity to better understand not only the mechanism of normal faulting but also its significance with respect to tectonics in northwestern Tibet.

The epicenter of the 2008 Yutian earthquake is located near the southern border of the Tarim Basin (Fig. 1), where the Altyn-Tagh Fault, a major sinistral strike–slip fault system in northern Tibet, meets the Karakax Fault (West Altyn-Tagh Fault) in northwestern Tibet (Styron et al., 2010; Tapponnier and Molnar, 1977; Taylor and Yin, 2009). To the southwest of the epicentral area, there is another ENE-striking sinistral strike–slip fault system, the Longmu–Gozha Co Fault (Fig. 1). It should be noted that the Ashikule volcano group, where the latest eruption was witnessed in 1951 (Global Volcanism Program, Smithonian Institution), is located at ~30 km to the north

* Corresponding author. Tel.: +81 11 706 2759.
E-mail address: furuya@mail.sci.hokudai.ac.jp (M. Furuya).

0040-1951/$ – see front matter © 2011 Elsevier B.V. All rights reserved.
doi:10.1016/j.tecto.2011.09.003

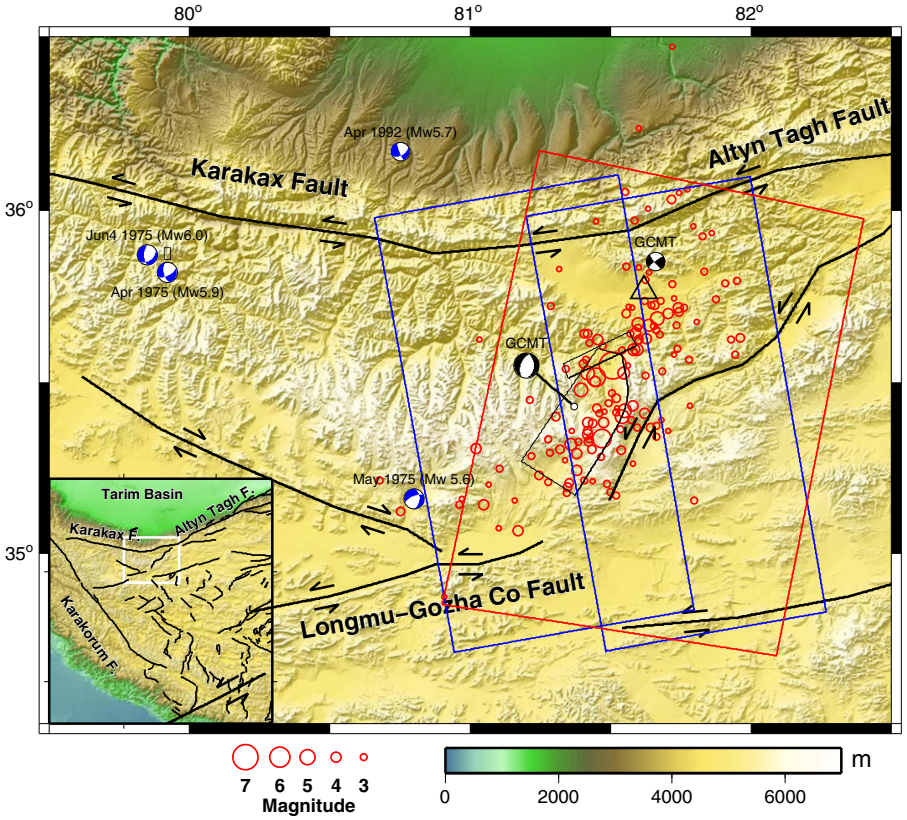

Fig. 1. Location map of the epicentral area of the Yutian earthquake and the regional topography. Main shock and aftershock locations from the International Seismological Centre are shown with red circles, and the centroid moment tensor (CMT) solution for the main shock (Mw 7.1) determined by Global CMT (GCMT) project is also shown. Previous earthquakes in the area are shown in blue and the mechanisms are based on Molnar and Chen (1983) for the three 1975 events and on GCMT for the 1992 event. Major fault traces are drawn from HimaTibetMap-1.0 by Styron et al. (2010): see also Taylor and Yin (2009). Three rectangles represent the areas observed by two ascending tracks of ALOS/PALSAR (blue) and one descending track of Envisat/ASAR (red). The Ashikule volcano group is located near the triangle. (For interpretation of the references to color in this figure legend, the reader is referred to the web version of this article.)

of the epicenter (Fig. 1). Although the Ashikule volcano group seems dormant at present, Liu and Maimaiti (1989) documented NS-trending Quaternary-active volcanoes and spatter cones. Because the existence of volcanoes could be used as indicators of tectonic stress orientation (e.g.. Nakamura, 1977), we may interpret Liu and Maimaiti's observation as reflecting an EW extensional stress field over the area. The EW extensional stress may be relevant to the generation of NS-striking normal fault earthquakes around the area. Moreover, based on isotopic and geochemical data for the trachyandesite samples at the Ashikule Basin, Cooper et al. (2002) concluded that it is unlikely that the magma was produced due to the subduction process, and that it was due to extension induced by the development of pull-apart basins along the major strike–slip faults.

Elliot et al. (2010) reported the crustal deformation signals associated with several normal faulting earthquakes in Tibet, using synthetic aperture radar (SAR) data sets. They developed fault slip distribution models using rectangular dislocation Green's functions devised by Okada (1992). For the 2008 Yutian earthquake, Elliot et al. (2010) presented three planar surfaces, based on their consideration of topography and surface rupture mapping using Advanced Spaceborne Thermal Emission and Reflection Radiometer (ASTER) imagery. However, their use of rectangular planar geometry generates mechanically incompatible overlaps in the fault model, because the observed data indicate that the fault geometry is non-planar. Moreover, Elliot et al. (2010) suggested two interpretations of the tectonic origin of the 2008 Yutian earthquake. In one interpretation, two ENE-striking left-lateral strike–slip faults in the Longmu–Gozha Co Fault system generated dilatational extension at a step-over region.

In the other interpretation, noting that the earthquake occurred in the highest region on earth when averaged over a 100 km scale, they also suggested that the extension regime conformed to the gravitational spreading model. Both interpretations can account for the extensional stress responsible for the normal faulting earthquake.

Although essential features of our crustal deformation observations are similar to those in Elliot et al. (2010), we show both InSAR and pixel offset data that were not presented in Elliot et al. Based on these observation data sets, we present a non-planar fault source model that is free from mechanically incompatible overlaps. While it is well known that Green's functions based on a triangular dislocation element (TDE) are useful to this end (e.g., Comninou and Dunders, 1975; Jeyakumaran et al., 1992; Yoffe, 1960), and Poly3D software has been widely used in the literature (Maerten et al., 2005; Thomas, 1993), we demonstrate our own approach for generating a non-planar fault model. Considering mechanical interaction of the nearby multiple faults, previous studies of nearby earthquakes (e.g., Molnar and Chen, 1983), and paleomagnetic data (Rumelhart et al., 1999), we discuss the possible implications for the present activity of the Karakax Fault.

2. Data analysis and results

2.1. Observation

We use ALOS/PALSAR data on two ascending paths and Envisat/ASAR data on one descending path to observe crustal deformation signals (Fig. 1); see Table 1 for the data sets. Our SAR data processing procedures are basically the same as those in our previous

Please cite this article as: Furuya, M., Yasuda, T., The 2008 Yutian normal faulting earthquake (Mw 7.1), NW Tibet: Non-planar fault modeling and implications for the Karakax Fault, Tectonophysics (2011), doi:10.1016/j.tecto.2011.09.003

Table 1
Details of the observed SAR data sets in Fig. 2.

Satellite	Orbit†	Path	Frame	Dates	Bperp (m)‡
ALOS	A	515	690–700	2008/01/26–2008/04/27	1175
ALOS	A	514	690–700	2008/02/24–2008/05/26	252
Envisat	D	477	2889–2907	2007/04/01–2008/04/20	−126

† A and D stand for ascending (mostly from the south to the north) and descending (from the north to the south) orbit. On both orbits, the SAR sensor looks to the right with an off-nadir angle of 34.3 and 23.5° for ALOS and Envisat, respectively.

‡ Orbit separation distance perpendicular to the radar line-of-sight. Units are in meters.

studies (Furuya et al., 2010; Kobayashi et al., 2009); we generated all the interferograms and pixel-offset data from level 1.0 for PALSAR and level 0 for ASAR data, using the commercial software package from Gamma Remote Sensing. To eliminate topographic fringes, we use the SRTM4 digital elevation model (DEM) (Jarvis et al., 2008) in which data gaps in the original Shuttle Radar Topography Mission (SRTM) data are filled. To correct for the orbital fringes, we use high-precision orbit data provided from Japan Aerospace exploration Agency (JAXA) for ALOS and DORIS-based orbit data from European Space Agency (ESA) for Envisat, and do not re-estimate them, because the orbit data are not the preliminary ones but the final high precision products. We acknowledge that errors in orbit data sometimes generate significant residual phase ramps and/or large-scale artifacts, and thus performed the error analysis below, suggesting that those errors did not substantially change the slip distribution results at shallower depth.

While interferometric SAR (InSAR) can detect range changes along the radar line-of-sight (LOS) with precision on the order of 2–3 cm, they do not give quantitative data about where interferometric coherence is lost and are less sensitive to the north–south component in 3D displacements. This is because the InSAR LOS direction is perpendicular to the satellite track, which is usually close to the north–south direction. Thus, since the precision is on the order of 15 cm or less (Fialko et al., 2001; Kobayashi et al., 2009), we also employ a pixel-offset tracking technique based on the intensity correlation of two SAR images (e.g., Michel et al., 1999; Tobita et al., 2001). We use the azimuth component of the pixel-offset data. Although these are helpful in identifying the surface rupture location, we do not use the range component of the pixel-offset data because it measures the same changes as InSAR data but is less precise. Although Envisat pixel-offset data were also generated, they were not used to invert the fault source model because they contained significant data gaps. This was probably because the lower spatial resolution in the original single look complex data as well as the long temporal separation did not generate a robust intensity correlation.

In Fig. 2, we show the observed (a) ALOS InSAR data along the western ascending path, (b) ALOS InSAR data along the eastern ascending path, (c) Envisat InSAR data along the descending path, and (d) ALOS azimuth offset data acquired on the same path and dates as in (a). We reduced the number of data points using the quadtree decomposition technique (e.g., Jónsson et al., 2002; Simons et al., 2002). In addition, we masked the mountain glacier signals in the azimuth offset data because they were not used for fault slip inversion; they will be reported elsewhere.

The broadscale signals in Fig. 2a–c indicate that the overall strike direction is oriented from NNE to SSW, as shown by Shao and Ji (2008) and suggested by the aftershock distribution in Fig. 1. However, the localized and large-amplitude signals in Fig. 2a and b, and the azimuth-offset data in Fig. 2d reveal that the strike direction is nearly NS and obviously different from the overall strike direction noted above. The maximum change in the radarline-of-sight (LOS) approached ~200 cm away from the radar LOS (Fig. 2a and b). In addition, the coherence loss immediately to the east of the largest-amplitude signals in Fig. 2a and b as well as the clear sign contrast in Fig. 2d indicate that the fault slip generated a surface rupture, which Elliot et al. (2010) confirmed using ASTER imagery. These observation results indicate that the earthquake fault surface geometry is curved, which strikes overall fromNNE to SSW but curves near the largest deformation zone. We found that the surface rupture is at least as much as 20-km long and is oriented almost NS. In addition, when compared to the local topography (Fig. 1), the surface rupture is located exactly at the west-dipping fault scarp, whose relative height is ~1000 m. The existence of the west-dipping fault scarp strongly suggests that normal faulting earthquakes caused by a similar mechanism must have occurred repeatedly.

In Fig. 1, we plot the aftershocks reported from the International Seismological Centre during the 8-day period from March 20 to March 27 including the main shock (International Seismological Centre, 2001). Overall, they are distributed from NNE to SSW. Six focal mechanisms are determined by the GCMT project for the aftershocks with Mw>5, and two indicate a strike–slip mechanism. The largest aftershock (Mw 5.2) on March 26 is located to the NE of the main shock, whose focal mechanism is also indicated in Fig. 1. This observation is consistent with our inferred fault slip distribution model noted below; the northern segment reveals a virtually strike–slip component alone at shallower depths.

2.2. Non-planar fault modeling

Although Okada's (1992) analytical solutions are useful for expressing ground displacements due to dislocation sources in a homogeneous elastic half space, they assume a rectangular dislocation element, and thus will generate mechanically incompatible gaps and/or overlaps if used to represent curviplanar fault source geometries (Maerten et al., 2005). While Poly3D software has been frequently employed (Maerten et al., 2005; Thomas, 1993), we discuss below how the MATLAB code by Meade (2007) allows us to perform the curved fault source modeling. In Meade's code, analytical solutions due to TDE were used to express displacements due to a non-planar fault surface (Comninou and Dunders, 1975; Jeyakumaran et al., 1992; Meade, 2007; Yoffe, 1960).

For this earthquake, we propose two fault segments as shown in Fig. 3. The southern segment is located such that the top edge can closely follow the observed surface rupture, the aftershock distribution, and the fault scarp (Figs. 1 and 2). Although its contribution is rather minor in the overall matching of observation and calculation, the northern segment is necessary for closely reproducing bull's-eye shaped fringes in the observed InSAR data (Fig. 2a and b), and is shown below to generate a left-lateral strike–slip with few dip slips, which is consistent with the largest Mw 5.2 aftershock noted above. Two pieces of information motivated us to introduce the northern segment. First, unless we introduced it, there arose significant misfit residuals near the observed bull's-eye-shaped InSAR data (Fig. 4 shows the calculated data and residuals without the northern segment). On comparing the residuals in Figs. 2 and 4, it is evident that the northern segment significantly contributes to both the ALOS and Envisat InSAR data. Elliot et al. (2010) also put a small northern segment in their model. We can identify significant residuals in their data (see Fig. 13 in Elliot et al., 2010) that are quite similar to the residuals in Fig. 4. We presume this is because the northern fault length is very short in Elliot et al. (2010). Second, as theoretical studies on dynamic rupture propagation over multiple fault segments have indicated (e.g., Oglesby, 2005 and the references therein), the long NE-striking northern segment increases the overlapped region of the two sinistral slip fault segments, which will more easily promote earthquake nucleation over the step-over and through-going ruptures across it. We believe that both northern and southern strike–slip segments are part of the NE-striking Altyn-Tagh and Longmu–Gozha Co Fault systems.

Please cite this article as: Furuya, M., Yasuda, T., The 2008 Yutian normal faulting earthquake (Mw 7.1), NW Tibet: Non-planar fault modeling and implications for the Karakax Fault, Tectonophysics (2011), doi:10.1016/j.tecto.2011.09.003

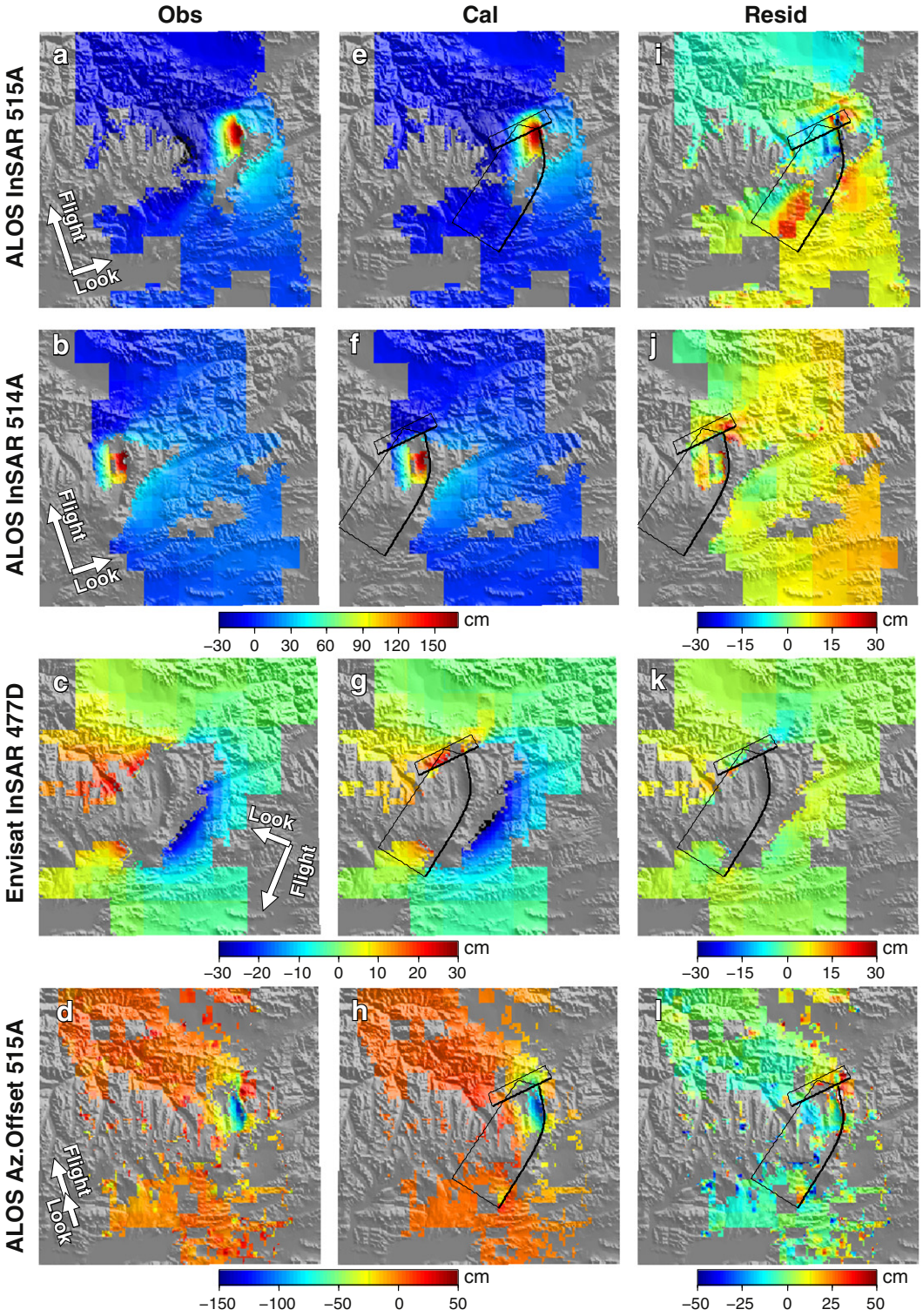

Fig. 2. (a–c) Observed unwrapped interferograms and (d) azimuth offset data for the 2008 Yutian earthquake derived from the flight and look directions shown in each panel; mountain glacier signals in (d) were masked. (e–h) Calculated interferograms and azimuth offset data corresponding to Fig. 2a–d, respectively. They are derived from the non-planar slip distribution model in Fig. 3. ALOS InSAR and azimuth offset data are a linear combination of 3D displacement components and equal to $0.616U_e+0.109U_n-0.780U_z$ and $-0.174U_e+0.985U_n$, respectively. Envisat InSAR data is equal to $-0.379U_e+0.081U_n-0.922U_z$; U_e, U_n, and U_z are eastward, northward, and upward positive displacement, respectively. Black lines indicate the plan view of the fault model in Fig. 3, where thick lines represent the top edge of the fault model. (i–l) Misfit residuals for each calculated data in Fig. 2e–h, respectively.

To generate triangular mesh coordinates to represent the fault geometry, we use a free mesh generation software, Gmsh (Geuzaine and Remacle, 2009). Triangular mesh generation is indispensable, even if one uses point source solutions (Okada, 1992) to represent curviplanar geometry; in other words, we do not have to rely on the analytical solutions for TDE. At the outset, we give 3D coordinates for 14 control points that are interpolated with splines to form each non-planar surface; see the circles in Fig. 3a.

We derived the fault configuration in Fig. 3 with a trial-and-error approach (e.g., Furuya et al., 2010), varying systematically the

Please cite this article as: Furuya, M., Yasuda, T., The 2008 Yutian normal faulting earthquake (Mw 7.1), NW Tibet: Non-planar fault modeling and implications for the Karakax Fault, Tectonophysics (2011), doi:10.1016/j.tecto.2011.09.003

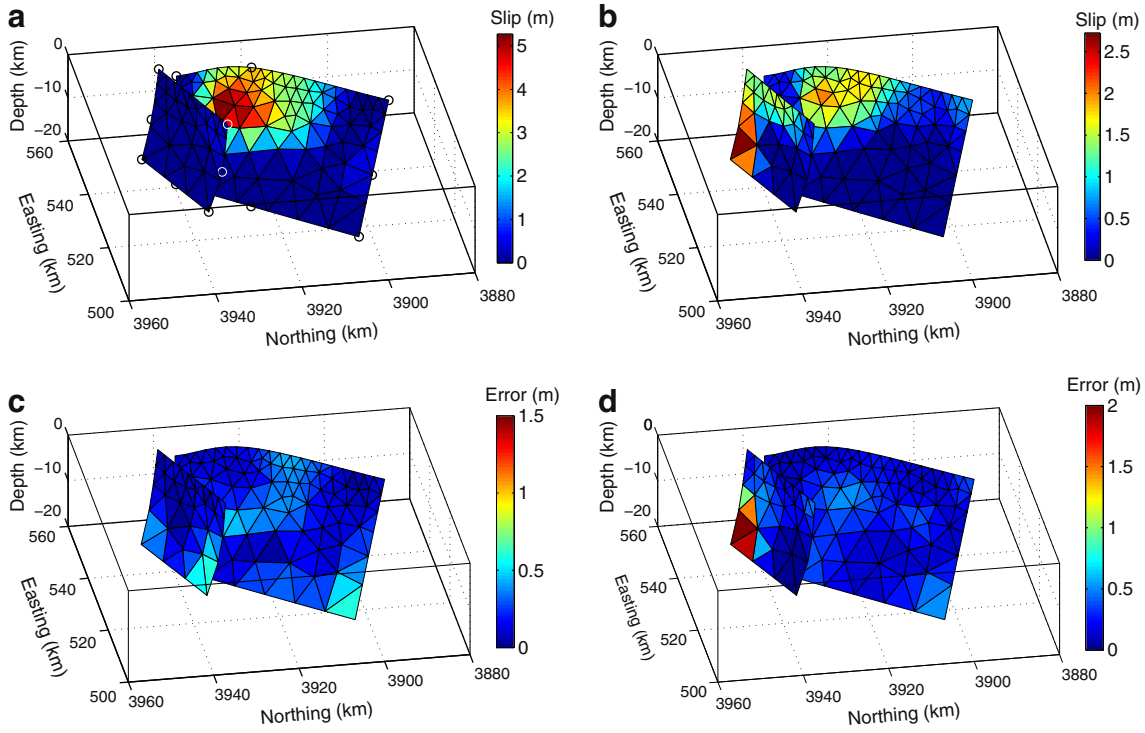

Fig. 3. Fault source model for the Yutian earthquake inverted from the observed data in Fig. 2; plan view is illustrated in Fig. 2. (a) Normal slip distribution. (b) Left-lateral slip distribution. (c) 1-sigma uncertainty for the normal fault slip. (d) 1-sigma uncertainty for the left-lateral slip. Circles at the edges of each fault segment represent the control points used to generate the 3D non-planar geometry and the mesh; two control points are invisible because they are on the back side of the northern segment.

horizontal location of the bottom control points and the 3D location of the middle-depth points. Were-calculated Green's function at each step, and derived a distributed slip solution and misfit residuals. We stopped our search for the configuration when no uninterpretable misfit residuals appeared. To avoid unnecessarily complicated fault geometry, the bottom edges were set straight in both segments, and the bottom depth of all the control points was assumed to be 20 km in both segments; the top edge of the northern and southern segment was fixed at depth of 1 km and at the surface, respectively. The dip angle in the northern segment was selected such that it would not deviate significantly from the southern segment. However, as the following error analysis indicates, the slip amplitude in the deeper portion is unreliable.

Because the resolution of the slip distribution decreases with depth (Bos and Spakman, 2003), we made the mesh size smaller (larger) at shallower (deeper) depth; the characteristic lengths were set at 2.5 km (7.0 km) at the shallowest (deepest) control points. Gmsh automatically generates 3D mesh coordinates at all nodes. From this, we can calculate Green's function for each slip patch.

In deriving the slip distribution, we applied both a smoothness constraint on the spatial slip distribution with the scale-dependent umbrella operator (Desbrun et al., 1999; Maerten et al., 2005) and a non-negativity constraint on the signs of the fault slip (Lawson and Hanson, 1974) in which only left-lateral and normal-fault slip components were allowed for the solution. The smoothness constraint can be implemented by computing the distance from the center of each triangular element to the adjacent triangular elements (Desbrun et al., 1999; Maerten et al., 2005). We assume that all the subsampled observational data are independent and the error covariance matrix is diagonal with uncertainties of 5 cm and 3 cm for the ALOS InSAR and Envisat InSAR, respectively, and 15 cm for the ALOS azimuth offset data (Kobayashi et al., 2009). Then, it is straightforward to invert the slip distribution as a linear problem (e.g., Fialko, 2004; Jónsson et al., 2002; Simons et al., 2002; Wright et al., 2003).

2.3. Fault slip distribution

The predicted data in Fig. 2e–h reproduce the observed features fairly well, and the misfit residuals are mostly less than 10 cm and 20 cm for InSAR and azimuth offset data, respectively. Although we can point out some broad and systematic misfit residuals in Fig. 2i–l, we do not think they represent any unmodeled deformation signals. For instance, there remain significant positive misfits as large as 20 cm in LOS to the SE in Fig. 2i. We interpret this as due to atropospheric noise, because neither Fig. 2j nor Fig. 2k shows such large misfit residuals at the same places. In addition, if we shift the top edge of the southern segment to the west, we cannot account for the Envisat InSAR data (Fig. 2c). Furthermore, the long-wavelength EW-trending slope in Fig. 2j is probably due to orbital errors and/or atmospheric noise.

Fig. 3a and b shows the inferred spatial distributions of the normal-fault and left-lateral slip components, respectively, and illustrate that the maximum slip at ~7-km depth took place where the fault surface bended from near NS strike to SW strike; this feature cannot be reproduced if one uses rectangular dislocation elements. While the bottom depth of the fault model is fixed at a depth of 20 km, a substantial part of the slip emanates from the surface to a depth shallower than 10 km. Near the northern end of the southern segment, only a minor slip component was derived. The northern segment revealed very few normal slip components (Fig. 3a) but showed significant left-lateral slip at the shallowest zone (Fig. 3b). While a large amplitude left-lateral slip is also very evident near the bottom of the northern segment (Fig. 3b), its amplitude does not exceed the error level (Fig. 3d). It is an artifact due to the presence of large-scale noises and the non-negativity constraint as discussed below.

Total moment of the earthquake is calculated to be 62×10^{18} Nm from the slip model in Fig. 3a and b, and becomes 56×10^{18} Nm if we exclude the artifactual strike–slip in Fig. 3b. The inferred moment is only3% larger than that estimated by Elliot et al. (2010). Because

Please cite this article as: Furuya, M., Yasuda, T., The 2008 Yutian normal faulting earthquake (Mw 7.1), NW Tibet: Non-planar fault modeling and implications for the Karakax Fault, Tectonophysics (2011), doi:10.1016/j.tecto.2011.09.003

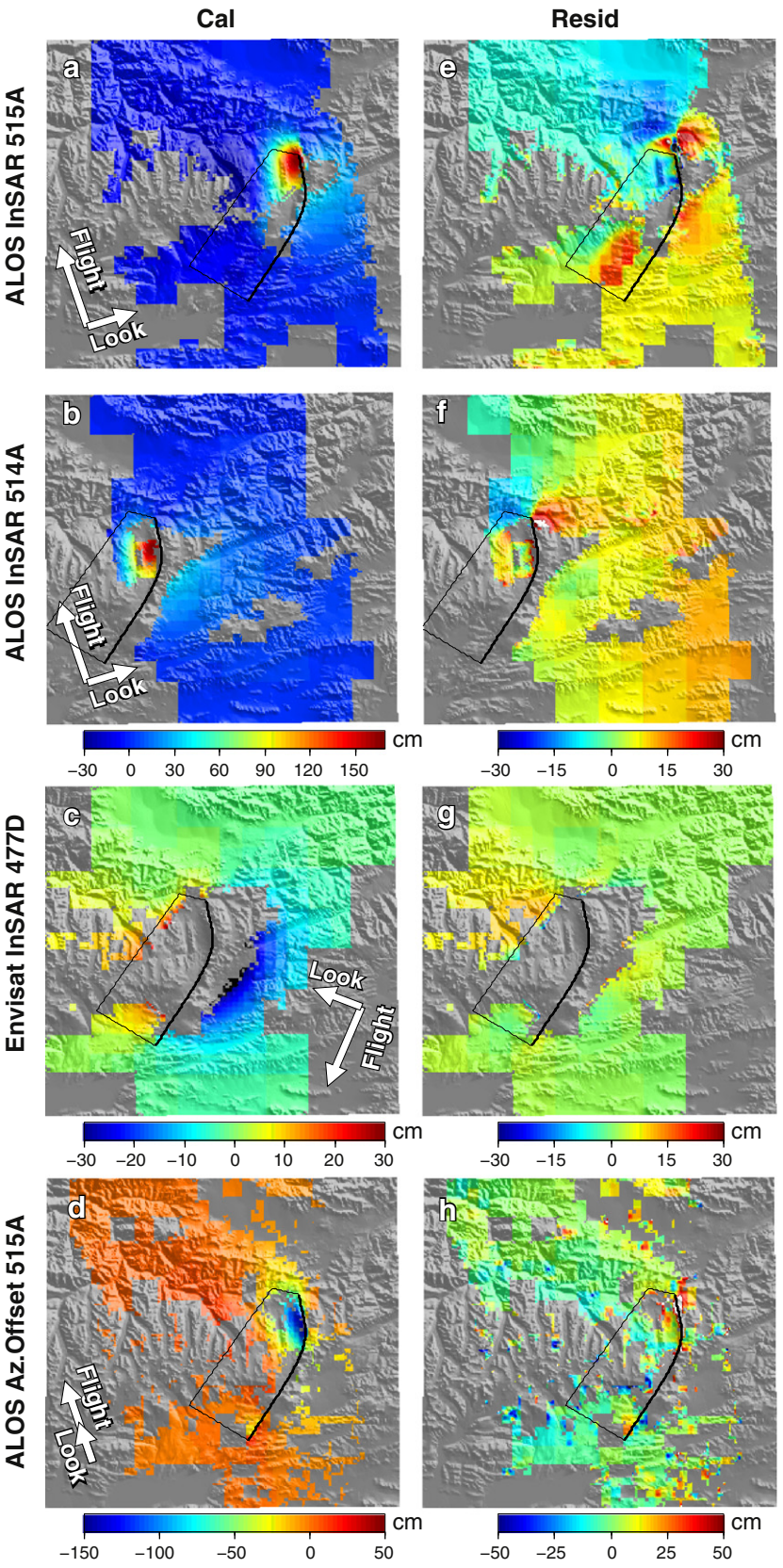

Fig. 4. (a–d) Calculated interferograms and azimuth offset data corresponding to the observed data in Fig. 2a–d, respectively. They are derived from the non-planar slip distribution model without the northern segment. Black lines indicate the plan view of the fault model without the northern segment. Although we derived the slip distribution without introducing the northern segment, the inferred slip distribution in the southern segment was nearly the same as that in Fig. 3. (e–h) Misfit residuals for each calculated data in Fig. 4a–d, respectively.

Please cite this article as: Furuya, M., Yasuda, T., The 2008 Yutian normal faulting earthquake (Mw 7.1), NW Tibet: Non-planar fault modeling and implications for the Karakax Fault, Tectonophysics (2011), doi:10.1016/j.tecto.2011.09.003

each TDE has different strike and dip angles in the non-planar fault model, we take the six largest slip patches to compare those angles with the ones in previous studies. The dip angles of the six patches range from 50° to 58°, and the strike angles range from 159° to 171°. The west-dipping GCMT nodal plane has 52° and 203° for the dip and strike angles, respectively. The dip angles for these largest slip patches are mostly consistent with that of GCMT, but the strike angles are different by as much as 30° or more. The second segment in Elliot et al. (2010) also has a strike angle of less than 170°. However, if we consider the entire fault slip distributions, the overall strike is obviously greater than 180° (Fig. 3a and b).

Fig. 3c and d are error estimates for normal-slip and left-lateral slips, respectively. These error estimates were derived by perturbing the calculated signals from the estimated slip distribution with synthetic 2D correlated noises and repeating the linear inversion 300 times to derive mean and standard deviations (Furuya et al., 2007, 2010; Wright et al., 2003); note that the estimated errors in Fig. 3c and d are always positive because of the non-negativity constraint. Fig. 3d shows large uncertainties near the bottom of the northern segment, and thus the large left-lateral slip near the bottom of the northern segment in Fig. 3b turns out to be unreliable.

In fact, even when we replaced the large left-lateral slip values near the bottom with zeros before perturbing the calculated signals, we could derive the large left-lateral slips and errors similar to those in Fig. 3b and d. Therefore, the systematically localized slips near the bottom in Fig. 3b are artifacts, and the uncertainties in Fig. 3d originate from our approach to infer the slip distribution. We point out that the non-negativity constraint in deriving the slip distribution causes the problem, because it will always explain any observed data with "positive" values regardless of signals or noises. Fig. 5 shows the slip distribution estimates and their errors derived without using the non-negativity constraint; we again replaced the large left-lateral slip values with zeros. Because we did not apply the constraint, Fig. 5a and b includes both negative and positive slip values. However, the spatial pattern of the derived slip distribution is consistent with those in Fig. 3a and b. Fig. 5c and d was generated by repeating the same procedure as that used in Fig. 3c and d without the non-negativity constraint. Fig. 5c and d illustrates that the error magnitudes of both normal-slip and left-lateral slips become comparable and more broadly distributed at a deeper zone. We speculate that the reason why the artifactual slip appears at the left-lateral deeper slip patches instead of other patches is that the large-scale noises in the observed data could be best "explained" by deeper patches, and that in the case of this earthquake the signals due to the normal faulting are overwhelmingly larger than those due to the strike–slip.

3. Discussion

3.1. Tectonic origin of the 2008 Yutian earthquake

Fig. 3 suggests that the Yutian earthquake rupture was nucleated in an EW-trending extensional stress field. As pointed out by Taylor and Yin (2009) and Elliot et al. (2010), we believe the EW-trending extensional stress is generated at a step-over region of two left-lateral en-echelon strike–slip fault systems, namely the Altyn-Tagh and Longmu–Gozha Co Fault systems. Furthermore, the study areas are broadly distributed step-over regions formed by the Altyn-Tagh and Longmu–Gozha Co Fault systems. The EW-trending extensional stress regime also seems relevant to the generation of the Ashikule volcano group as noted before. It is an unlikely coincidence that young active intra-continental volcanoes exist at the location. In our fault source model shown in Fig. 1, the smaller northern segment and the southern segment probably belong to a part of the Altyn-Tagh and Longmu–Gozha Co Fault systems, respectively. Besides the normal faulting slip, the left-lateral strike–slips on the ENE-striking Altyn-Tagh and Longmu–Gozha Co Fault systems are reasonable candidates where NS shortening occurs.

Elliot et al. (2010) also suggested a gravitational spreading model as first proposed by Molnar and Tapponnier (1978), because the epicentral area is the highest region on the earth. However, Molnar and Tapponnier's model was originally proposed to account for an extensional graben and normal fault that are dominant in middle to

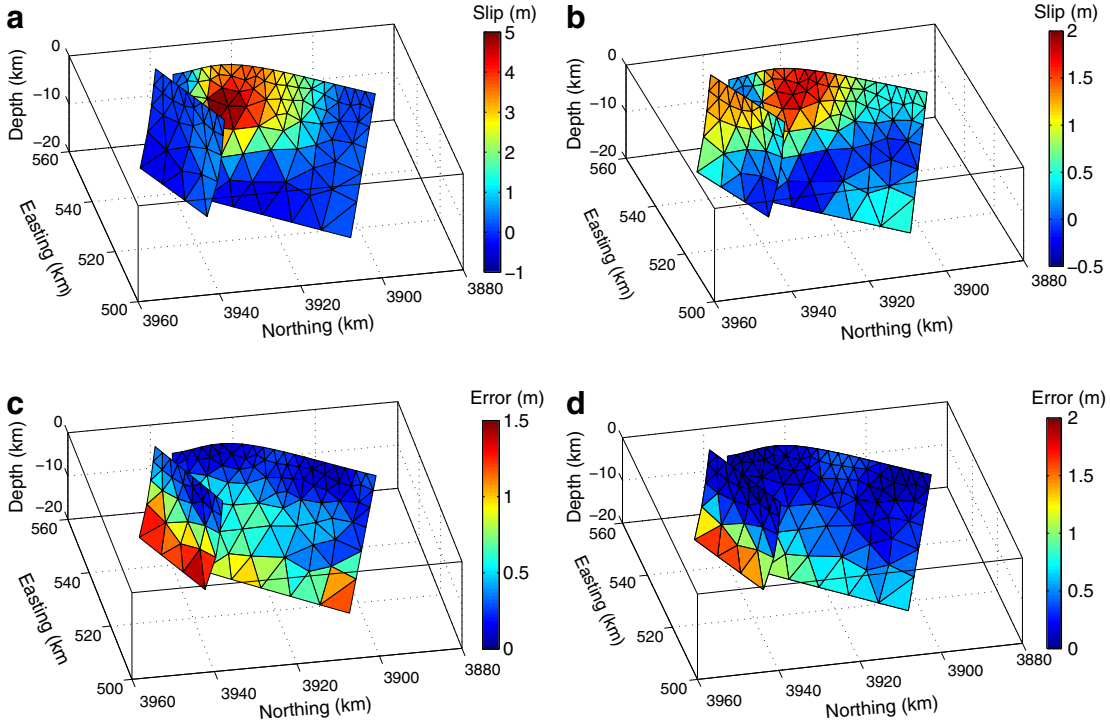

Fig. 5. Fault source model for the Yutian earthquake inverted from the observed data in Fig. 2 without constraining the signs of slip vectors. (a) Normal slip distribution. (b) Left-lateral slip distribution. (c) 1-sigma uncertainty for the normal fault slip. (d) 1-sigma uncertainty for the left-lateral slip.

Please cite this article as: Furuya, M., Yasuda, T., The 2008 Yutian normal faulting earthquake (Mw 7.1), NW Tibet: Non-planar fault modeling and implications for the Karakax Fault, Tectonophysics (2011), doi:10.1016/j.tecto.2011.09.003

southern Tibet, where strike–slip faulting earthquakes are rare (Armijo et al., 1986; Copley et al., 2011). In northern Tibet, on the other hand, strike–slip faulting is the primary tectonic regime, and normal faulting earthquakes are concentrated only around the study area (see Fig. 1 in Copley et al., 2011). As Copley et al. (2011) regard the elevation of the plateau rather uniform, there are other regions in northern Tibet that are equally high in their elevation but lack in normal faulting. Although we do not reject the gravitational spreading model, we consider that the step-over region model would be more likely for the 2008 Yutian earthquake.

3.2. Current activity of the Karakax Fault

Although Lin et al. (2008) suggest a right-lateral slip sense of the Karakax Fault, which can apparently explain the EW-extensional stress and is mechanically feasible, the focal mechanisms of the previously recorded earthquakes do not support a right-lateral slip sense. Below, we speculate the current location of the Karakax Fault stands in the present-day tectonic setting.

As noted in Section 2, the largest normal faulting slip of the 2008 event occurred at the west-dipping fault scarp on the surface, suggesting that normal faulting earthquakes have repeatedly occurred over time. The Coulomb stress changes exerted on the Karakax Fault by the NS-striking normal faulting earthquakes must have been repeatedly suppressed the left-lateral slip behavior of the Karakax Fault. Although the left-lateral slip sense is widely known (e.g., Peltzer et al., 1989), we speculate that the geologically determined slip rate and sense may not be applicable at present. The absence of purely left-lateral strike–slip earthquakes in the upper crust to the west of 79.5°E along the Karakax Fault may be consistent with the interpretation, although we need a long-term geological slip rate history and a more complete paleoseismological study along the fault.

Using Landsat images, Peltzer et al. (1989) observed offsets of geomorphic features across the Karakax Fault and inferred a left-lateral slip rate of ~20 mm/yr. However, based on campaign-based GPS measurements, Shen et al. (2001) reported 7 ± 3 mm/yr, which is much smaller than the geological measurements. More recently, Wright et al. (2004) reported 5 ± 5 mm/yr from their InSAR data, indicating that even the sense of on-going slip remains uncertain. While large discrepancies between geological and geodetic measurements have been observed at the Altyn-Tagh Fault over the past decades (Bendick et al., 2000; Peltzer et al., 1989; Shen et al., 2001), recent geologic studies indicate lower slip rates that are more consistent with the GPS-derived rate of ~9 mm/yr (Cowgill et al., 2009; Yin et al., 2002).

If substantial slip along the Altyn-Tagh Fault is transferred to the Longmu–Gozha Co Fault, which is south across this normal-fault system, the slip rate of the Karakax Fault could be less than that of the adjoining Altyn-Tagh Fault to the east.

Over the past three decades, there occurred four earthquakes in the areas, whose focal mechanisms could be derived (Fig. 1). All show both left-lateral strike–slip and normal faulting, and none indicate a thrust faulting mechanism with the rare exception of much deeper events (e.g., Chen and Yang, 2004; Huang et al., 2011; Molnar and Chen, 1983; Molnar and Lyon-Caen, 1989). Although we need much longer-term earthquake history over the area, few thrust faulting earthquakes in northern Tibet indicate that the NS-shortening of Tibet must be presently accommodated in the conjugate strike–slip faulting, with left-lateral slip on NE-striking planes and right-lateral slip on NW-striking planes (e.g., Hatzfeld and Molnar, 2010). Therefore, it should be noted that the WNW striking Karakax Fault is mechanically incompatible with left-lateral slip, although almost all the previous literature regards it as an extension of the left-lateral slipping Altyn-Tagh Fault (e.g., Avouac and Tapponnier, 1993).

We do not dispute the geologically determined left-lateral slip sense. Based on paleomagnetic declination data, Rumelhart et al. (1999) showed that the West Kunlun Shan underwent a clockwise vertical axis rotation and suggested that the left-slip Karakax Fault may have formed as an accommodation zone between the West Kunlun Shan and the Karakorum Mountains. This interpretation can reconcile the mechanically incompatible slip sense known at the Karakax Fault; it also suggests that the Karakax Fault is not simply an extension of the Altyn-Tagh Fault (see also Yin et al., 2002). Rumelhart et al. (1999) further indicated that the Altyn-Tagh Fault has not rotated significantly, and thus suggested a "pivot point for rotation" around the western end of the Altyn-Tagh Fault. We speculate that the pivot point would be more broadly distributed and could correspond to the previously-mentioned step-over region.

4. Conclusions

Using ALOS/PALSAR and Envisat/ASAR data, we show the crustal deformation signals associated with the 2008 Yutian normal faulting earthquake. Although the overall strike direction is from NNE to SSW, both InSAR and azimuth offset data indicate that the strike direction changes near the largest deformation zone. We describe how to perform a non-planar fault source modeling using the TDE. A substantial part of the slip was revealed on the west-dipping normal faulting slip. We demonstrate that in the presence of large-scale noises, artifactual slips can be derived under a so-called non-negativity constraint, providing us with a caveat on the slip inversion results based on SAR data. For the earthquakes with normal-faulting and a left-lateral strike–slip mechanism to occur in this area, we believe that the present-day slip rate at the Karakax Fault might be much smaller than that along the Altyn-Tagh Fault at present.

Acknowledgment

PALSAR level 1.0 data used in this study were provided by the PALSAR Interferometry Consortium to Study our Evolving Land surface (PIXEL) under a cooperative research contract with the JAXA. The ownership of PALSAR data belongs to JAXA and the Ministry of Economy, Trade and Industry (METI). ASAR level 0 data are courtesy of the European Space Agency. This study was supported partly by KAKENHI (19340123). Discussions with B. H. Fu initiated this study. We thank Roland Bürgmann and an anonymous reviewer for their critical review and constructive comments.

References

Armijo, R., Tapponnier, P., Mercier, J.L., Tong-Lin, H., 1986. Quaternary Extension in Southern Tibet: Field Observations and Tectonic Implications. Journal of Geophysical Research 91 (B14), 13803–13872.

Avouac, J.P., Peltzer, G., 1993. Active Tectonics in Southern Xinjiang, China: Analysis of Terrace Riser and Normal Fault Scarp Degradation Along the Hotan-Qira Fault System. Journal of Geophysical Research 98 (B12), 21773–21807.

Avouac, J.P., Tapponnier, P., 1993. Kinematic Model of Active Deformation in Central Asia. Geophysical Research Letters 20 (10), 895–898.

Bendick, R., Bilham, R., Freymueller, J., Larson, K., Yin, G., 2000. Geodetic evidence for a low slip rate in the Altyn Tagj fault system. Nature 404, 69–72.

Bos, A.G., Spakman, W., 2003. The resolving power of coseismic surface displacement data for fault slip distribution at depth. Geophysical Research Letters 30 (21), 2110. doi:10.1029/2003GL017946.

Chen, W.P., Yang, Z.H., 2004. Earthquakes beneath the Himalayas and Tibet: Evidence for strong lithospheric mantle. Science 304, 1949–1952. doi:10.1126/science.1097324.

Comninou, M., Dunders, J., 1975. The angular dislocation in a half space. Journal of Elasticity 5, 203–216.

Cooper, K.M., Reid, M.R., Dunbar, N.W., McIntosh, W.C., 2002. Origin of mafic magmas beneath northwestern Tibet: Constraints from 230Th–238U disequilibria. Geochemistry, Geophysics, Geosystems 3, 1065. doi:10.1029/2002GC000332.

Copley, A., Avouac, J.P., Wernicke, B.P., 2011. Evidence for mechanical coupling and strong Indian lower crust beneath southern Tibet. Nature 472, 79–81. doi:10.1038/nature09926.

Cowgill, E., Gold, R.D., Chen, X., Wang, X.F., Arrowsmith, J.R., Southon, J., 2009. Low Quarternary slip rate reconciles geodetic and geologic rates along the Altyn Tagh fault, northwestern Tibet. Geology 37 (7), 647–650. doi:10.1130/G25623A.

Desbrun, M., Meyer, M., Schroder, P., Barr, A.H., 1999. Implicit fairing of irregular meshes using diffusion and curvature flow. SIGGRAPH 99, 317–324.

Please cite this article as: Furuya, M., Yasuda, T., The 2008 Yutian normal faulting earthquake (Mw 7.1), NW Tibet: Non-planar fault modeling and implications for the Karakax Fault, Tectonophysics (2011), doi:10.1016/j.tecto.2011.09.003

Ekström, G., Dziewonski, A.M., Maternovskaya, N.N., Nettles, M., 2005. Global seismicity of 2003: centroid moment-tensor solutions for 1087 earthquakes. Physics of the Earth and Planetary Interiors 148, 327–351.
Elliot, J.R., Walters, R.J., England, P.C., Jackson, J.A., Li, Z., Parsons, B., 2010. Extension on the Tibetan plateau: recent normal faulting measured by InSAR and body wave seismology. Geophysical Journal International 183, 503–535. doi:10.1111/j.1365-246X.2010.04754.x.
England, P., Houseman, G., 1989. Extension During Continental Convergence, With Application to the Tibetan Plateau. Journal of Geophysical Research 94 (B12), 17,561–17,579.
Fialko, Y., 2004. Probing the mechanical properties of seismically active crust with space geodesy: Study of the coseismic deformation due to the 1992 7.3 Landers (southern California) earthquake. Journal of Geophysical Research 109, B03307. doi:10.1029/2003JB002756.
Fialko, Y., Simons, M., Agnew, D., 2001. The complete (3-D) surface displacement field in the epicentral area of the 1999 MW 7.1 Hector Mine Earthquake, California, from space geodetic observations. Geophysical Research Letters 28 (16), 3063–3066.
Furuya, M., Mueller, K., Wahr, J., 2007. Active salt tectonics in the Needles District, Canyonlands (Utah) as detected by interferometric synthetic aperture radar and point target analysis: 1992–2002. Journal of Geophysical Research 112, B06418. doi:10.1029/2006JB004302.
Furuya, M., Kobayashi, T., Takada, Y., Murakami, M., 2010. Fault Source Modeling of the 2008 Wenchuan Earthquake Based on ALOS/PALSAR Data. Bulletin of the Seismological Society of America 100 (5B), 2750–2766. doi:10.1785/0120090242.
Geuzaine, C., Remacle, J.F., 2009. Gmsh: a three-dimensional finite element mesh generator with built-in pre- and post-processing facilities. International Journal for Numerical Methods in Engineering 79 (11), 1309–1331.
Global Volcanism Program, Smithonian Institution, a. http://www.volcano.si.edu/world/volcano.cfm?vnum=1004-03-.
Hatzfeld, D., Molnar, P., 2010. Comparisons of the kinematics and deep structures of the Zagros and Himalaya and of the Iranian and Tibetan plateaus and geodynamic implications. Reviews of Geophysics 48, RG2005. doi:10.1029/2009RG000304.
Huang, G.C.D., Roecker, S.W., Levin, V., 2011. Lower-crustal earthquakes in the West Kunlun range. Geophysical Research Letters 38, L01314. doi:10.1029/2010GL045893.
International Seismological Centre, 2001. On-line Bulletin. Internatl. Seis. Cent, Thatcham, United Kingdom. http://www.isc.ac.uk.
Jarvis, A., Reuter, H.I., Nelson, A., Guevara, E., 2008. Hole-filled seamless SRTM data V4, International Centre for Tropical Agriculture (CIAT). available from http://srtm.csi.cgiar.org.
Jeyakumaran, M., Rudnicki, J.W., Keer, L.M., 1992. Modeling slip zones with triangular dislocation elements. Bulletin of the Seismological Society of America 82, 2153–2169.
Jónsson, S., Zebker, H., Segall, P., Amelung, F., 2002. Fault slip distribution of the 1999 Mw 7.1 Hector Mine, California, earthquake, estimated from satellite radar and GPS measurements. Bulletin of the Seismological Society of America 92, 1377–1389.
Kobayashi, T., Takada, Y., Furuya, M., Murakami, M., 2009. Locations and types of ruptures involved in the 2008 Sichuan earthquake inferred from SAR image matching. Geophysical Research Letters 36, L07302. doi:10.1029/2008GL036907.
Lawson, C.L., Hanson, R.J., 1974. Solving Least Squares Problems. Prentice-Hall.
Lin, A., Kano, K.I., Guo, J., Maruyama, T., 2008. Late Quaternary activity and dextral strike–slip movement on the Karakax Fault Zone, northwest Tibet. Tectonophysics 453, 44–62. doi:10.1016/j.tecto.2007.04.013.
Liu, J., Maimaiti, Y., 1989. Distribution and ages of Ashikule volcanoes on the West Kunlun Mountains, west China. Bulletin of Glacier Research 7, 187–190.
Maerten, F., Resor, P., Pollard, D., Maerten, L., 2005. Inverting for slip on three-dimensional fault surfaces using angular dislocations. Bulletin of the Seismological Society of America 95, 1654–1665. doi:10.1785/0120030181.
Meade, B.J., 2007. Algorithms for the calculation of exact displacements, strains, and stresses for triangular dislocation elements in a uniform elastic half space. Computers and Geosciences 33, 1064–1075. doi:10.1016/j.cageo.2006.12.003.
Michel, R., Avouac, J.-P., Taboury, J., 1999. Measuring ground displacements from SAR amplitude images: Application to the Landers earthquake. Geophysical Research Letters 26, 875–878.
Molnar, P., Chen, W.P., 1983. Focal depth and fault plane solutions of earthquakes under the Tibetan Plateau. Journal of Geophysical Research 88 (B2), 1180–1196.
Molnar, P., Lyon-Caen, H., 1989. Fault plane solutions of earthquakes and active tectonics of the Tibetan Plateau and its margins. Geophysical Journal International 99, 123–153.
Molnar, P., Tapponnier, P., 1978. Active tectonics of the Tibet. Journal of Geophysical Research 83 (B11), 5361–5375.
Nakamura, K., 1977. Volcanoes as possible indicators of tectonic stress orientation — principle and proposal. Journal of Volcanology and Geothermal Research 2, 1–16.
Oglesby, D.D., 2005. The Dynamics of Strike–Slip Step-Overs with Linking Dip–Slip Faults. Bulletin of the Seismological Society of America 95, 1604–1622. doi:10.1785/0120050058.
Okada, Y., 1992. Internal deformation due to shear and tensile faults in a half-space. Bulletin of the Seismological Society of America 82, 1018–1040.
Peltzer, G., Tapponnier, P., Armijo, R., 1989. Magnitude of Late Quaternary Left-Lateral Displacements Along the North Edge of Tibet. Science 246, 1285–1289.
Rumelhart, P.E., Yin, A., Cowgill, E., Butler, R., Zhang, Q., Wang, X.F., 1999. Cenozoic vertical-axis rotation of the Altyn Tagh fault system. Geology 27 (9), 819–822.
Shao, G., Ji, C., 2008. Preliminary Result of the Mar 20, 2008 Mw 7.14 Xinjiang Earthquake. UCSB, California, USA. http://www.geol.ucsb.edu/faculty/ji/big_earthquakes/2008/03/20/Xinjiang_206.html.
Shen, Z.K., Wang, M., Li, Y., Jackson, D.D., Yin, A., Dong, D., Fang, P., 2001. Crustal deformation along the Altyn Tagh fault system, western China, from GPS. Journal of Geophysical Research 106 (B12), 30607–30621.
Simons, M., Fialko, Y., Rivera, L., 2002. Coseismic Deformation from the 1999 Mw 7.1 Hector Mine, California, Earthquake as Inferred from InSAR and GPS Observations. Bulletin of the Seismological Society of America 92, 1390–1402. doi:10.1785/0120000933.
Styron, R., Taylor, M., Okoronkwo, K., 2010. Database of Active Structures From the Indo-Asian Collision. Eos 91 (20), 181–182.
Sun, J., Shen, Z., Xu, X., Bürgmann, R., 2008. Synthetic normal faulting of the 9 January 2008 Nima (Tibet) earthquake from conventional and along-track SAR interferometry. Geophysical Research Letters 35, L22308. doi:10.1029/2008GL035691.
Tapponnier, P., Molnar, P., 1977. Active faulting and tectonics in China. Journal of Geophysical Research 82 (20), 2905–2930.
Taylor, M., Yin, A., 2009. Active structure of the Himalayan–Tibetan orogen and their relationships to earthquake distribution, contemporary strain field, and Cenozoic volcanism. Geosphere 5, 199–214. doi:10.1130/GES00217.1.
The Global CMT Project, 2008. The Global CMT Project. available from http://www.globalcmt.org/.
Thomas, A.L., 1993. Poly3D: a three-dimensional, polygonal element, displacement discontinuity boundary element computer program with applications to fractures, faults, and cavities in the earth's crust, M. S. Thesis, Stanford University, 221 pp.
Tobita, M., Murakami, M., Nakagawa, H., Yarai, H., Fujiwara, S., Rosen, P.A., 2001. 3-D surface deformation of the 2000 Usu eruption measured by matching of SAR images. Geophysical Research Letters 28, 4291–4294.
Wright, T.J., Lu, Z., Wicks, C., 2003. Source model for the Mw 6.7, 23 October 2002, Nenana Mountain Earthquake (Alaska) from InSAR. Geophysical Research Letters 30. doi:10.1029/2003GL018014.
Wright, T.J., Parsons, B., England, P.C., Fielding, E.J., 2004. InSAR Observations of Low Slip Rates on the Major Faults of Western Tibet. Science 305, 236–239. doi:10.1126/science.1096388.
Yin, A., 2000. Mode of Cenozoic east–west extension in Tibet suggesting a common origin of rifts in Asia during the Indo-Asian collision. Journal of Geophysical Research 105 (B9), 21,745–21,760.
Yin, A., Kapp, P.A., Murphy, M.A., Manning, C.E., Harrison, T.M., Grove, M., Lin, D., Xi-Guang, D., Cun-Ming, W., 1999. Significant late Neogene east–west extension in northern Tibet. Geology 27 (9), 787–790.
Yin, A., Rumelhart, P.E., Butler, R., Cowgill, E., Harrison, T.M., Foster, D.A., Ingersoll, R.V., Wang, Q., Zhou, X.Q., Wang, X.F., Hanson, A., Raza, A., 2002. Tectonic history of the Altyn Tagh fault system in northern Tibet inferred rom Cenozoic sedimentation. Geological Society of America Bulletin 114 (10), 1257–1295.
Yoffe, E., 1960. The angular dislocation. Philosophical Magazine 5, 161–175.

Please cite this article as: Furuya, M., Yasuda, T., The 2008 Yutian normal faulting earthquake (Mw 7.1), NW Tibet: Non-planar fault modeling and implications for the Karakax Fault, Tectonophysics (2011), doi:10.1016/j.tecto.2011.09.003